applied sciences

MDPI

Article

Deep Learning-Assisted Segmentation, Multiparametric MRI Radiomics, and Clinical Features for Recurrence Risk Stratification in Young-Age Breast Cancer: A Prospective Pilot Study

Ga Eun Park [1], Jeongmin Lee [2], Eun Jeong Min [3], Seok Ho Hahm [4] and Sung Hun Kim [1,*]

[1] Department of Radiology, Seoul Saint Mary's Hospital, College of Medicine, The Catholic University of Korea, Seoul 06591, Republic of Korea
[2] Department of Radiology, Samsung Medical Center, Sungkyunkwan University School of Medicine, Seoul 06351, Republic of Korea
[3] Department of Medical Life Sciences, College of Medicine, The Catholic University of Korea, Seoul 06591, Republic of Korea
[4] Department of Medical Sciences, Graduate School, The Catholic University of Korea, Seoul 06591, Republic of Korea
* Correspondence: rad-ksh@catholic.ac.kr; Tel.: +82-2-2258-1455

Abstract

Purpose: To develop an exploratory prognostic model integrating multiparametric MRI radiomics and clinical features for recurrence risk stratification in young-age breast cancer (YABC). Materials and Methods: In this prospective single-institution cohort, women under 40 years with invasive breast cancer were enrolled between March 2017 and August 2019 and followed for at least 5 years. Tumor and contralateral fibroglandular tissue were segmented on multiparametric breast MRI using a deep learning-assisted model. Radiomic features were extracted and reduced via principal component analysis, and then integrated with clinical variables. Recurrence-free survival (RFS) was compared between risk groups using Kaplan–Meier analysis and the log-rank test. Internal assessment used 1000 bootstrap resamples to evaluate selection stability and optimism-corrected performance. Results: Fifty women (mean age, 34.8 ± 3.6 years) were included, and 11 patients (22%) had recurrence during a median follow-up of 64.5 months. Triple-negative subtype and lower T1_cancer3 showed strong exploratory associations, whereas lower ADC_FGT4 and larger pathologic tumor size showed weaker associations. Risk groups differed in RFS (log-rank $p = 0.0022$). Bootstrap analysis showed moderate selection stability, with preserved discrimination but limited calibration stability after optimism correction. Conclusions: MRI radiomics combined with clinical factors may provide complementary prognostic information for recurrence risk stratification in YABC, warranting validation in larger independent cohorts.

Keywords: young-age breast cancer; deep learning-assisted segmentation; multiparametric MRI radiomics; risk stratification; recurrence prediction

Check for updates

Academic Editors: Mehmed M. Kantardzic and Mehmet Akif Gulum

Received: 23 July 2026
Revised: 5 September 2026
Accepted: 8 September 2026
Published: 9 September 2026

Copyright: © 2026 by the authors. Licensee MDPI, Basel, Switzerland. This article is an open access article distributed under the terms and conditions of the Creative Commons Attribution (CC BY) license.

1. Introduction

In recent decades, advances in screening and treatment have substantially improved breast cancer survival. Despite these gains, both the incidence and mortality of breast cancer have been rising rapidly in many Asian countries [1–3]. Of particular concern is breast cancer among women under 40 years of age—commonly referred to as young-age

breast cancer (YABC)—who are generally excluded from population-based breast cancer screening programs. According to the Korean Statistical Information Service (KOSIS), YABC accounted for approximately 9% of all female breast cancers in 2020, with its incidence nearly doubling over the past two decades from 63 to 129 cases per 100,000 women [4–6]. YABC often presents with aggressive features, is more frequently diagnosed at an advanced stage, and is associated with worse outcomes, underscoring the need for careful risk assessment to guide management [5,7,8].

Breast MRI is the most sensitive imaging modality for breast cancer detection and is routinely used for preoperative planning. Beyond its diagnostic role, multiparametric MRI offers excellent soft tissue contrast and the ability to capture diverse tissue characteristics through various sequences, not only of the primary tumor but also of the underlying breast parenchyma [9]. YABC more frequently presents with aggressive pathologic features such as higher histologic grade, increased Ki-67 index, and a higher proportion of the triple-negative breast cancer (TNBC) subtype. However, previous studies suggest that the underlying tumor biology of YABC-associated TNBC does not differ substantially from that of TNBC in other age groups [10–12]. Because all YABC patients are premenopausal, they typically demonstrate significantly higher fibroglandular tissue (FGT) content and background parenchymal enhancement (BPE) on breast MRI than postmenopausal women, suggesting potential differences in the microenvironment of the breast parenchyma [13,14].

Radiomics provides high-dimensional quantitative descriptors of shape, texture, and the microenvironment of both the tumor and FGT that extend beyond human visual perception [15–17]. Previous studies have demonstrated its utility in differentiating benign from malignant lesions, classifying molecular subtypes, predicting response to neoadjuvant chemotherapy, and estimating prognosis [18–24]. More recently, integration with genomic data has given rise to radiogenomics, further expanding its potential in precision oncology [25–27]. However, prognostic radiomics studies have largely focused on the primary tumor, and relatively little attention has been given to radiomic characteristics of the contralateral fibroglandular tissue, particularly in young women with breast cancer.

Given the distinctive age-related breast parenchymal characteristics of YABC, we hypothesize that radiomics features derived from both tumor and parenchyma, when integrated with clinical variables, may provide additional prognostic information in this population. Therefore, we prospectively evaluated a YABC cohort and developed an exploratory prognostic model.

2. Materials and Methods

2.1. Study Population

The study protocol was approved by the Institutional Review Board of Seoul St. Mary's Hospital. Written informed consent was obtained from all participants prior to enrollment in accordance with the principles of the Declaration of Helsinki. This prospective single-center study was conducted between March 2017 and August 2019, targeting women under 40 years of age with newly diagnosed invasive breast cancer. A total of 53 patients consented to participate. During follow-up, one patient was lost to follow-up, one was excluded because of cancer segmentation failure due to poor lesion enhancement on MRI, and one was excluded after liver metastasis was identified within 1 month after surgery, suggesting clinically occult metastatic disease at baseline. Consequently, 50 patients were included in the final analysis, and all were followed for at least five years, except for patients whose follow-up ended earlier because of death (Figure 1).

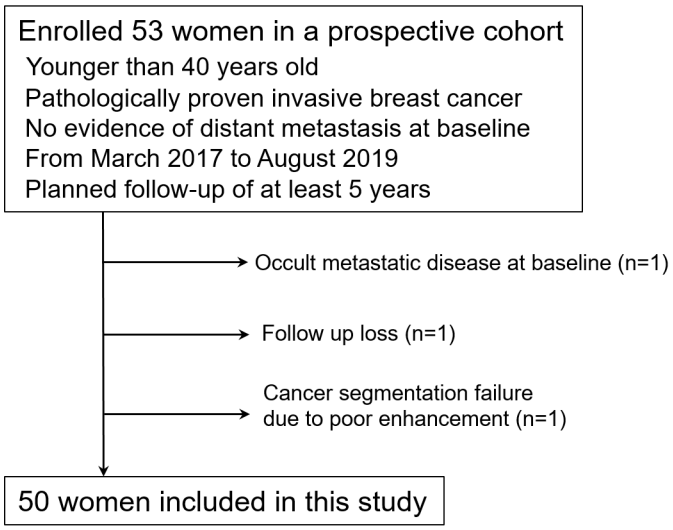


Figure 1. Flowchart of study population.

2.2. Clinical and Pathological Information

Medical records of all enrolled patients were reviewed. Clinical information collected included the patient's age at diagnosis, date of surgery, date of last outpatient visit, date of disease recurrence, and details of treatments received, including surgery, chemotherapy, and radiation therapy. Pathologic data included histologic grade, hormone receptor (HR) status, human epidermal growth factor receptor 2 (HER2) status, Ki-67 proliferation index, and pathologic TNM staging according to the American Joint Committee on Cancer (AJCC) 7th edition. BRCA mutation status was also recorded when available. Recurrence was defined as the first occurrence of any of the following events occurring after surgery: ipsilateral breast recurrence, axillary lymph node recurrence, or distant metastasis. Recurrent disease was confirmed pathologically when biopsy was feasible. In cases where biopsy was not possible, imaging modalities such as computed tomography (CT) or positron emission tomography-computed tomography (PET-CT) were used to establish the diagnosis. Recurrence-free survival was calculated from the date of surgery to the date of the first documented recurrence. Patients without recurrence were censored at the date of their last clinical follow-up. No patient died before experiencing recurrence. Follow-up duration was defined as the interval from surgery to the last clinical follow-up or death.

2.3. MR Image Acquisition

All breast MRI examinations were performed preoperatively. In patients who received neoadjuvant chemotherapy, MRI was performed before initiation of systemic treatment. Breast MRI examinations were performed in the prone position using a 3.0-T scanner (Ingenia, Philips Medical Systems, Best, The Netherlands) with a dedicated eight-channel phased-array coil. The protocol included axial T2-weighted turbo spin-echo imaging, pre-contrast T1-weighted high-resolution isotropic volume examination (THRIVE), dynamic contrast-enhanced fat-suppressed T1-weighted imaging after intravenous injection of 0.1 mmol/kg gadobutrol. Diffusion-weighted imaging (DWI) was also obtained using two b values (0, 1000 s/mm^2), and apparent diffusion coefficient (ADC) maps were calculated with a monoexponential model. Detailed acquisition parameters are provided in Supplementary Table S1.

2.4. Automatic 3D Segmentation for Cancer and FGT and Radiomics Feature Extraction

Previously developed deep learning-assisted models [28,29] were applied to segment the tumor and the FGT of the contralateral normal breast. Four MRI sequences were ana-

lyzed: subtracted T1-weighted images (T1WI) obtained by subtracting pre-contrast images from early phase post-contrast images; T2-weighted images (T2WI); DWI (b = 1000 s/mm^2); and ADC maps. All three-dimensional segmentation masks were reviewed by an experienced radiologist. When minor inaccuracies were identified in parts of the automatically generated segmentation masks, localized manual corrections were performed.

Using the finalized segmentation masks, a comprehensive set of radiomic features was extracted from each tumor and FGT mask across the four imaging sequences. Before feature extraction, T1WIs were used as the reference images. T2WIs and DWIs acquired at b = 0 s/mm^2 were rigidly registered to the T1WIs using a six-degree-of-freedom transformation, and the corresponding transformation derived from the b = 0 s/mm^2 images was applied to the ADC maps. All images and segmentation masks were resampled to an isotropic voxel size of 1 × 1 × 1 mm^3 using B-spline interpolation for images and nearest-neighbor interpolation for masks. Image intensities were z-score normalized and subsequently multiplied by 100. Gray-level discretization was performed using a fixed bin width of 10. Three-dimensional radiomic features were extracted from the entire segmented volume using PyRadiomics version 3.0 implemented in Python version 3.6. Only features derived from the original images were included. In total, 107 quantitative features were extracted from each image-mask combination, including shape (n = 14), first-order statistics (n = 18), and texture features (n = 75). Thus, eight sequence–region combinations were analyzed, yielding 856 candidate radiomic features before dimensionality reduction.

2.5. Feature Selection with Dimensionality Reduction

Principal component analysis (PCA) was applied to reduce dimensionality and eliminate multicollinearity among raw radiomic features from multiparametric MRI. Radiomic features were extracted separately for each sequence–region combination, comprising subtracted T1-weighted, T2-weighted, diffusion-weighted (b = 1000 s/mm^2), and ADC images for both the tumor and the contralateral FGT, yielding eight combinations with 107 features per combination and 856 candidate features in total. Within each sequence–region combination, features were z-score-standardized using the mean and standard deviations, and PCA was then performed independently for that combination rather than on the pooled feature set. Orthogonal principal components (PCs) were derived as linear combinations of the original features within each combination, and components were retained until the cumulative explained variance first exceeded 80%, yielding four to five components per combination and 38 components in total. Because PCA was performed separately for each combination, components derived from the same analysis are orthogonal by construction, whereas components derived from different combinations may remain correlated. Pairwise correlations among the retained components were therefore examined to reduce cross-combination redundancy. For any pair with an absolute correlation coefficient of 0.70 or greater, the component with the higher mean absolute correlation with all remaining components was removed, and the correlation matrix was recomputed after each removal until no pair exceeded the threshold. Neither survival time nor recurrence status was used at any point in this procedure. Two of the 38 components were removed under this criterion, leaving 36 components. The removal sequence is provided in Supplementary Table S2.

2.6. Model Building

The retained PCs and clinical variables were entered as candidate predictors. All candidate predictors were scaled to unit standard deviation using full-cohort values so that the penalty was applied comparably across predictors measured on different scales.

Least absolute shrinkage and selection operator (LASSO) Cox regression was used to select predictors associated with recurrence-free survival. The penalty parameter was selected by five-fold cross-validation stratified on recurrence status, using the concordance index as the cross-validation criterion, with the value at its optimum retained; the random seed and fold assignment were fixed. Predictors with non-zero penalized coefficients were subsequently entered into an unpenalized multivariable Cox proportional hazards model fitted in the same cohort. Where one indicator variable of a multi-level categorical variable was selected, the remaining indicators of that variable were also included so that the reference category was preserved. Ties in event times were handled using the Efron approximation. β coefficients are from the unpenalized multivariable Cox model refitted after LASSO-based predictor selection. Hazard ratios are reported in original units for clinical variables and per one standard deviation for principal components. To facilitate interpretation of the radiomic principal components included in the final Cox model, the 10 original radiomic features with the highest absolute loadings for each component are provided in Supplementary Table S3. The proportional hazard assumption was assessed using scaled Schoenfeld residuals. There were no missing values among the retained variables. A risk score was calculated for each patient as the linear predictor of the fitted Cox model, and patients were stratified into low- and high-risk groups at the median risk score.

2.7. Bootstrap Internal Validation

Given the limited sample size of this single prospective cohort (n = 50), independent validation through random splitting of the dataset was not considered feasible. Internal assessment was therefore performed using bootstrap resampling, with the principal component representation derived from the full cohort held fixed so that a given component retained the same meaning throughout.

Selection stability was assessed using 1000 event-stratified bootstrap resamples, in which recurrent and non-recurrent patients were resampled separately with replacement to preserve the number of events across resamples. Within each resample, correlation-based filtering, penalty selection, and LASSO-Cox selection were repeated from the beginning. For each candidate predictor, the proportion of resamples in which it was selected was recorded, together with the distribution and sign of its coefficient among resamples in which it was selected. The full-data β and conditional bootstrap β values are penalized LASSO coefficients on the standardized predictor scale. Conditional bootstrap β values summarize coefficients only among bootstrap resamples in which the corresponding predictor had a non-zero coefficient.

Optimism in model performance was estimated using 1000 unstratified bootstrap resamples. Within each resample, correlation-based filtering, penalty selection, LASSO-Cox selection, and refitting of the unpenalized Cox model were repeated from the beginning. Each resulting model was applied both to its own bootstrap resample and to the original cohort, and the difference in performance between the two was taken as the optimism for that resample. The mean optimism across resamples was then used to derive optimism-corrected performance estimates. Discrimination was assessed using Harrell's concordance index, calibration using the calibration slope, and predictive accuracy at prespecified time points of 3 and 5 years using the Brier score with inverse probability of censoring weighting. Iterations in which a model could not be fitted were recorded as failures rather than imputed, and the number of valid iterations was reported for each metric.

2.8. Statistical Analysis

Continuous variables were compared using Student's *t* test or the Wilcoxon rank-sum test when normality was violated; categorical variables were compared using Chi-square or Fisher's exact test when ≥25% of cells had expected counts ≤5. When multiple comparisons were performed in descriptive tables, we applied Benjamini–Hochberg false discovery rate (FDR) adjustment and reported both raw and adjusted *p*-values.

Baseline characteristics between the defined risk groups were compared using appropriate statistical tests, and recurrence-free survival was assessed using Kaplan–Meier analysis with the log-rank test. Because the risk score and the median threshold were both derived within the same cohort, these survival comparisons are presented as exploratory descriptions of the stratification observed in the study population rather than as independent evidence of predictive performance.

All statistical analyses were performed using R version 4.4.3 (R Foundation for Statistical Computing, Vienna, Austria). A two-sided *p*-value of less than 0.05 was considered statistically significant.

3. Results

Among the 50 patients finally enrolled, the mean age was 34.8 ± 3.6 years. Based on pathology reports, most patients were classified as stage I (48%, 24/50) or stage II (40%, 20/50). Four patients who received neoadjuvant chemotherapy achieved a pathologic complete response and were confirmed as stage 0. In terms of molecular subtypes across the entire cohort, the majority were HR positive/HER2 negative (64%, 32/50), followed by HER2 positive (20%, 10/50), and TNBC (16%, 8/50). Additional patient characteristics are summarized in Table 1.

Table 1. Baseline patient clinical and pathologic characteristics.

Variable	Total (n = 50)	Recurrence (n = 11)	Non-Recurrence (n = 39)	*p*-Value	Adjusted *p*-Value
Age at diagnosis (years)	34.8 ± 3.6	34.5 ± 3.9	34.9 ± 3.6	0.733	0.834
BRCA mutation				1	1
Negative	13 (26.0)	3 (27.3)	10 (25.6)		
Positive	8 (16.0)	2 (18.2)	6 (15.4)		
Not applicable	29 (58.0)	6 (54.5)	23 (59.0)		
Pathologic tumor size (cm)	1.74 ± 1.41	2.47 ± 1.82	1.54 ± 1.22	0.087	0.406
Pathologic nodal status				0.424	0.721
No	38 (76.0)	7 (63.6)	31 (79.5)		
Yes	12 (24.0)	4 (36.4)	8 (20.5)		
Stage				0.759	0.834
0	4 (8.0)	0 (0)	4 (10.3)		
I	24 (48.0)	5 (45.5)	19 (48.7)		
II	20 (40.0)	6 (54.5)	14 (35.9)		
III	2 (4.0)	0 (0)	2 (5.1)		
Histologic grade				0.190	0.485
Well	10 (20.0)	1 (9.1)	9 (23.0)		
Moderate	17 (34.0)	2 (18.2)	15 (38.5)		
Poorly	23 (46.0)	8 (72.7)	15 (38.5)		
Ki-67 (%)	41.0 ± 27.7	52.9 ± 28.4	37.6 ± 26.9	0.143	0.485

Table 1. *Cont.*

Variable	Total (n = 50)	Recurrence (n = 11)	Non-Recurrence (n = 39)	*p*-Value	Adjusted *p*-Value
Estrogen receptor				0.197	0.485
Positive	40 (80.0)	7 (63.6)	33 (84.6)		
Negative	10 (20.0)	4 (36.4)	6 (15.4)		
Progesterone receptor				0.424	0.721
Positive	38 (76.0)	7 (63.6)	31 (79.5)		
Negative	12 (24.0)	4 (36.4)	8 (20.5)		
HER2				0.424	0.721
Positive	10 (20.0)	1 (9.1)	9 (23.1)		
Negative	40 (80.0)	10 (90.9)	30 (76.9)		
Molecular subtypes				0.133	0.485
HR positive/HER2 negative	32 (64.0)	6 (54.5)	26 (66.6)		
HER2 positive	10 (20.0)	1 (9.1)	9 (23.1)		
TNBC	8 (16.0)	4 (36.4)	4 (10.3)		
Neoadjuvant chemotherapy				0.445	0.721
Yes	13 (26.0)	4 (36.4)	9 (23.1)		
No	37 (74.0)	7 (63.6)	30 (76.9)		
Breast operation				0.476	0.721
Breast conserving surgery	36 (72.0)	7 (63.6)	29 (74.4)		
Mastectomy	14 (28.0)	4 (36.4)	10 (25.6)		
Adjuvant chemotherapy				0.166	0.485
Yes	21 (42.0)	7 (63.6)	14 (35.9)		
No	29 (58.0)	4 (36.4)	25 (64.1)		
Radiation therapy				1	1
Yes	44 (88.0)	10 (90.9)	34 (87.2)		
No	6 (12.0)	1 (9.1)	5 (12.8)		

Values are presented as mean ± standard deviation, median [range] or number (percentage). Adjusted *p*-values were corrected for multiple comparisons using the Benjamini–Hochberg method.

The median follow-up duration for all patients after surgery was 64.5 months (range, 10–84 months). During the follow-up period, 11 patients experienced recurrence, with a median time to recurrence of 13.9 months (range, 4–71 months) after surgery. Of these, 7 patients had locoregional recurrence involving the ipsilateral breast or axilla. The remaining 4 patients presented with distant metastasis at the time of recurrence. During the follow-up period, three patients died due to metastatic breast cancer. Regarding molecular subtypes among the 11 patients with recurrence, 6 had HR positive/HER2 negative, 4 had TNBC, and 1 had HER2 positive type.

Clinical and pathologic characteristics of the low- and high-risk groups defined by the combined radiomics–clinical model are summarized in Table 2. A total of 50 patients were analyzed, of whom 25 were classified into the low-risk group and 25 into the high-risk group. Molecular subtype distribution also significantly differed before FDR adjustment ($p = 0.007$; Adjusted $p = 0.065$). TNBC was observed only in the high-risk group (32.0%), whereas the HR-positive/HER2-negative subtype was predominant in the low-risk group (76.0%). Histologic grade distribution differed between groups, with poorly differentiated

tumors being more frequent in the high-risk group (64.0% vs. 28.0%, $p = 0.033$), although this did not remain statistically significant after adjustment (adjusted $p = 0.185$). Ki-67 was higher in the high-risk group (51.1 ± 28.7% vs. 30.8 ± 23.0%, $p = 0.014$), but the difference did not reach significance after adjustment (adjusted $p = 0.098$). No statistically significant differences were noted in age at diagnosis, pathologic tumor size, pathologic nodal status, stage, type of surgery, radiotherapy, chemotherapy, or neoadjuvant therapy (adjusted $p > 0.05$ for all).

Table 2. Clinical and pathologic characteristics of low- and high-risk groups as defined by the combined model.

Variable	Low-Risk (n = 25)	High-Risk (n = 25)	*p*-Value	Adjusted *p*-Value
Recurrence	1 (4.0)	10 (40.0)	0.002	0.028
Age at diagnosis (years)	34.8 ± 3.08	34.8 ± 4.18	0.590	0.787
Pathologic tumor size (cm)	1.60 ± 1.22	1.89 ± 1.59	0.515	0.721
Pathologic nodal status			0.508	0.721
No	20 (80.0)	18 (72.0)		
Yes	5 (20.0)	7 (28.0)		
Stage			0.623	0.793
0	1 (4.0)	3 (12.0)		
I	14 (56.0)	10 (40.0)		
II	9 (36.0)	11 (44.0)		
III	1 (4.0)	1 (4.0)		
Histologic grade			0.033	0.185
Well	6 (24.0)	4 (16.0)		
Moderate	12 (48.0)	5 (20.0)		
Poorly	7 (28.0)	16 (64.0)		
Ki-67 (%)	30.8 ± 23.0	51.1 ± 28.7	0.014	0.098
Molecular subtypes			0.007	0.065
HR positive/HER2 negative	19 (76.0)	13 (52.0)		
HER2 positive	6 (24.0)	4 (16.0)		
TNBC	0 (0.0)	8 (32.0)		
Neoadjuvant chemotherapy			0.333	0.717
Yes	5 (20.0)	8 (32.0)		
No	20 (80.0)	17 (68.0)		
Breast operation			0.208	0.485
Breast conserving surgery	20 (80.0)	16 (64.0)		
Mastectomy	5 (20.0)	9 (36.0)		
Adjuvant chemotherapy			0.774	0.834
Yes	10 (40.0)	11 (44.0)		
No	15 (60.0)	14 (56.0)		
Radiation therapy			0.667	0.812
Yes	23 (92.0)	21 (84.0)		
No	2 (8.0)	4 (16.0)		

Values are presented as mean ± standard deviation or number (percentage). Adjusted *p*-values were corrected for multiple comparisons using the Benjamini–Hochberg method.

When both clinical variables and radiomics features were incorporated, multivariable Cox proportional hazards analysis was performed using predictors selected through the LASSO procedure (Table 3). Because the variables entered into the Cox model had been selected in a data-driven manner, the resulting *p*-values were interpreted as exploratory rather than confirmatory. Using the HR-positive/HER2-negative subtype as the reference, TNBC showed an exploratory association with a higher risk of recurrence (hazard ratio [HR] = 8.09, 95% confidence interval [CI]: 1.35–48.52, exploratory $p = 0.022$). Among the radiomics-derived principal components, T1_cancer3, derived from subtracted T1WI with cancer segmentation, showed an exploratory inverse association with recurrence risk (HR = 0.25, 95% CI: 0.10–0.65, exploratory $p = 0.004$). ADC_FGT4 and pathologic tumor size showed weaker associations with recurrence (HR = 0.57, 95% CI: 0.31–1.05, exploratory $p = 0.070$; and HR = 1.63, 95% CI: 0.92–2.88, exploratory $p = 0.096$, respectively). The HER2-positive subtype, T1_cancer1, T1_cancer4, and T2_cancer3 did not show clear evidence of association with recurrence (exploratory $p > 0.10$). Patients were further stratified into low- and high-risk groups according to the combined model-derived risk score. Baseline characteristics between the two risk groups were compared using appropriate statistical tests, and recurrence-free survival was evaluated using Kaplan–Meier analysis with the log-rank test. The high-risk group showed a substantially lower recurrence-free survival (RFS) than the low-risk group, with a significant separation of the Kaplan–Meier curves (log-rank $p = 0.0022$; Figure 2). Given that both the risk score and the cutoff were derived within the same cohort, this finding was considered exploratory and descriptive of the observed risk stratification.

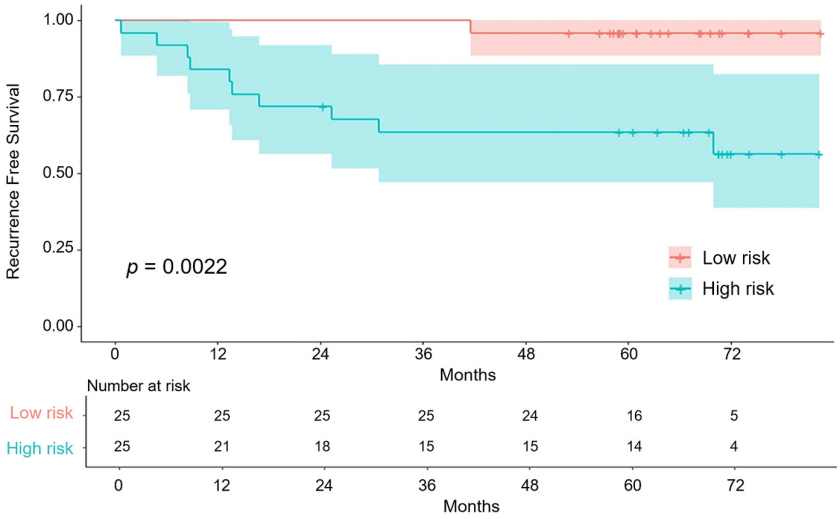


Figure 2. Kaplan–Meier curves showing recurrence-free survival according to risk group derived from the combined radiomics-clinical model. The low-risk group (red) and high-risk group (blue) are displayed with 95% confidence interval bands. Recurrence-free survival differed significantly between the two groups (log-rank $p = 0.0022$).

Internal validation using bootstrap resampling demonstrated variable selection stability and quantified optimism in model performance. Across 1000 event-stratified bootstrap resamples, the final-model predictors showed variable inclusion frequencies ranging from 10.9% to 72.1% (Table 4). T1_cancer3 showed the highest overall inclusion frequency (72.1%), followed by T2_cancer3 (67.6%), TNBC (63.9%), T1_cancer4 (55.2%), pathologic tumor size (51.1%), and ADC_FGT4 (45.9%). When selected, the direction of the regression coefficients was highly consistent with that observed in the full-data model, with sign consistency ranging from 98.0% to 100% among predictors for which this measure was

applicable. The conditional bootstrap coefficients also showed the same direction as the corresponding full-data coefficients.

Table 3. Multivariable Cox regression model after LASSO-based predictor selection.

Variables	Unpenalized β	HR (95% CI)	Exploratory *p*-Value
Molecular subtypes			
HR positive/HER2 negative (ref)	-	1	-
HER2 positive	0.5586	1.75 (0.13–23.44)	0.673
TNBC	2.0908	8.09 (1.35–48.52)	0.022
Pathologic tumor size	0.4858	1.63 (0.92–2.88)	0.096
T1_cancer1	0.2780	1.32 (0.46–3.80)	0.606
T1_cancer3	−1.3742	0.25 (0.10–0.65)	0.004
T1_cancer4	−0.6835	0.50 (0.19–1.34)	0.171
ADC_FGT4	−0.5644	0.57 (0.31–1.05)	0.070
T2_cancer3	0.6993	2.01 (0.64–6.34)	0.233

ref: reference; HR: Hazard ratio; CI: Confidence interval.

Table 4. Bootstrap Assessment of LASSO predictor-selection Stability and Penalized Coefficient Consistency.

Predictor	Full-Data Penalized β	Conditional Penalized β Median (Q1, Q3)	Filtering Survival (%)	Overall Inclusion (%)	Sign Consistency (%)
TNBC	0.2453	0.538 (0.252, 0.967)	—	63.9	99.5
HER2 positive	0.000	−0.194 (−0.555, −0.014)	—	10.9	—
Pathologic tumor size	0.1553	0.476 (0.212, 0.883)	—	51.1	99.6
T1_cancer3	−0.4166	−0.618 (−1.171, −0.295)	100	72.1	99.9
T1_cancer4	−0.0495	−0.427 (−0.812, −0.220)	99.9	55.2	100
T1_cancer1	0.0243	0.365 (0.168, 0.756)	76.7	26.7	100
ADC_FGT4	−0.0568	−0.376 (−0.647, −0.201)	94.4	45.9	98
T2_cancer3	0.3176	0.454 (0.232, 0.855)	96.9	67.6	100

Bootstrap-based optimism correction showed that model performance was lower than the apparent estimates derived from the original cohort (Table 5). Harrell's C-index decreased from 0.895 in the apparent model to 0.717 after optimism correction. The Brier score increased from 0.054 to 0.147 at 3 years and from 0.080 to 0.191 at 5 years. The optimism-corrected calibration slope was 0.160, compared with an apparent slope of 1.00, indicating considerable optimism in the apparent model performance and limited calibration stability.

Table 5. Apparent and Bootstrap Optimism-Corrected Performance of the Prognostic Model.

Performance Metric	Apparent Performance	Optimism-Corrected Performance	Number of Valid Bootstrap Replicates
Harrell's C-index	0.895	0.717	990
Brier score at 3 years	0.054	0.147	986
Brier score at 5 years	0.08	0.191	987
Calibration slope	1	0.160	987

4. Discussion

In this prospective cohort study of YABC patients, we explored a prognostic model integrating multiparametric breast MRI-derived radiomics features with clinical variables. The combined model identified TNBC and a radiomics-derived principal component from contrast-enhanced T1-weighted imaging as the variables showing the strongest exploratory associations with recurrence, while ADC-derived contralateral FGT features and pathologic tumor size showed weaker associations. The model also separated patients into low- and high-risk groups with significantly different RFS. However, because both the risk score and the cutoff were derived within the same cohort, this risk-group separation should be interpreted as an exploratory description of the stratification observed in the study population rather than as independent evidence of predictive performance.

In this study, we used a deep learning-assisted model for automatic segmentation of both the primary tumor and contralateral FGT across multiple MRI sequences. Although occasional minor manual corrections were required for the automated segmentations, this approach substantially reduced the burden of fully manual segmentation while providing a standardized framework for radiomics extraction. Notably, our analysis incorporated not only tumor regions but also the contralateral breast parenchyma, allowing for exploration of individual breast tissue characteristics as potential prognostic markers. This may be particularly relevant in YABC, in which both tumor biology and the surrounding breast environment may contribute to recurrence risk. Previous prognostic breast MRI radiomics studies have largely focused on intratumoral or peritumoral imaging features, including studies evaluating disease-free survival in patients with invasive breast cancer and recurrence risk in young women with breast cancer [30,31]. Although radiomic analysis of contralateral fibroglandular tissue has recently been explored for breast cancer phenotyping, including prediction of triple-negative breast cancer, its potential prognostic relevance remains relatively underexplored [32].

Although raw radiomics features could be directly entered into the model, their high degree of correlation warranted a dimensionality reduction approach before fitting the survival model. PCA offers several advantages, including transforming highly correlated variables into a smaller set of orthogonal principal components within each sequence-region combination, and mitigating the risk of overfitting in the context of a small sample size. However, this approach inevitably reduces direct interpretability because each principal component represents a weighted combination of multiple radiomics features rather than a single imaging feature. Accordingly, the biological meaning of individual components should be interpreted cautiously. Although reliance on individual radiomics features does not necessarily guarantee greater biological interpretability, future studies with larger datasets may allow for more transparent feature selection and independent assessment of reproducible component-level patterns [33].

Among the clinical variables included in the combined model, TNBC showed a strong exploratory association with a higher risk of recurrence compared with HR-positive/HER2-negative subtype (HR = 8.09, exploratory $p = 0.022$), consistent with the well-established aggressive clinical behavior of TNBC [34,35]. In contrast, HER2-positive disease did not show clear evidence of an association with recurrence in the fitted model. This may partly reflect the effectiveness of contemporary HER2-targeted therapies [36,37], including the routine use of dual HER2 blockade in our institution. However, the wide confidence intervals observed for subtype-specific hazard ratios reflect the limited number of events and preclude firm conclusions regarding differences among molecular subtypes.

Among the radiomics-derived PCs, T1_cancer3, derived from subtracted contrast-enhanced T1WI with tumor segmentation, showed the strongest exploratory inverse association with recurrence risk (HR = 0.25, exploratory $p = 0.004$). Contrast-enhanced T1WI is

the principal sequence for evaluating breast tumor vascularity, enhancement characteristics, and intratumoral heterogeneity [9], and this component may therefore capture aspects of the tumor enhancement phenotype that are relevant to prognosis. ADC_FGT4, derived from ADC maps of contralateral FGT, also showed an inverse association with recurrence, although the association was weaker (HR = 0.57, exploratory $p = 0.070$). Previous studies have shown that diffusion characteristics of normal breast parenchyma are reproducible and may be associated with breast density and hormonal factors [38–41]. These two PCs may reflect tumor heterogeneity and microenvironmental characteristics of the breast parenchyma. However, because the association did not meet conventional significance thresholds and arose from a data-driven selection procedure, this observation should be considered hypothesis-generating.

The bootstrap analyses provided additional information regarding both predictor stability and model performance. Across 1000 event-stratified bootstrap resamples, several predictors showed moderate selection frequencies, with T1_cancer3 showing the highest overall inclusion frequency, followed by T2_cancer3 and TNBC. When predictors were selected, the direction of their coefficients was highly consistent with that observed in the full-data model. These findings suggest that the direction of association for several variables was relatively stable, although the variation in inclusion frequencies indicates that the exact composition of the fitted model remained sensitive to resampling. Optimism correction substantially reduced the apparent performance of the model. Harrell's C-index decreased from 0.895 in the original cohort to 0.717 after bootstrap correction, while the Brier score increased from 0.054 to 0.147 at 3 years and from 0.080 to 0.191 at 5 years. The optimism-corrected calibration slope was 0.16, markedly lower than the ideal value of 1.0. Together, these findings indicate considerable optimism in the apparent model performance and limited calibration stability. The current model should therefore be regarded as exploratory and hypothesis-generating rather than as a clinically validated prognostic tool.

This prospective study has several limitations. First, this was a single-center pilot study based on a small cohort with a limited number of recurrence events. Therefore, the present analysis was not intended to establish a definitive prognostic model, but rather to explore whether multiparametric MRI-derived radiomics and clinical variables may contain potentially useful prognostic information in YABC. Although YABC represents a clinically important subgroup, patients younger than 40 years constitute only a small proportion of the overall breast cancer population, making the prospective accumulation of large event-rich cohorts challenging. Second, PCA was used to reduce dimensionality and collinearity, allowing highly correlated radiomics features to be summarized into a smaller number of orthogonal components. Although this may reduce the direct interpretability of individual features, it provides a practical approach for modeling high-dimensional radiomics data in a limited cohort. The risk score and cutoff were derived from the same cohort; thus, the observed Kaplan–Meier separation supports the potential of the model for risk stratification within the present cohort, although independent validation is required. Third, the absence of an independent validation set reflects the constraints of a small prospective sample and may limit generalizability. Internal validation was therefore performed using bootstrap resampling to assess variable-selection stability and to estimate optimism in model performance. However, bootstrap validation cannot substitute for external validation, and the substantial reduction in performance after optimism correction underscores the considerable risk of overfitting. In addition, the PCA representation was derived from the full cohort and held fixed during bootstrap resampling. Therefore, variability arising from PCA estimation was not incorporated, and the internal assessment may underestimate the total optimism of the complete modeling pipeline. Lastly, although we used multiparametric MRI radiomics combined with clinical factors, the extracted

radiomics features may be sensitive to variations in imaging protocols, scanner types, and segmentation accuracy. While all images were acquired on the same 3.0-T scanner and segmentation was reviewed with manual correction when needed, these steps may not fully eliminate variability in real-world settings.

Future studies should validate these findings in larger, multicenter cohorts with independent datasets and greater numbers of recurrence events. External validation should assess calibration as well as discrimination and determine whether the same radiomics-derived components retain prognostic value across scanners and imaging protocols. If reproducible, integration of MRI radiomics into risk models could complement genomic and histopathological data, advancing toward a more individualized risk assessment in YABC.

In conclusion, this prospective exploratory study suggests that clinical factors and multiparametric breast MRI-derived radiomics may provide complementary prognostic information in YABC. These findings are hypothesis-generating and warrant validation in larger independent cohorts.

Supplementary Materials: The following supporting information can be downloaded at https://www.mdpi.com/article/10.3390/app16188946/s1, Table S1: Detailed MRI Acquisition Parameters; Table S2: Principal Components Removed by Correlation-Based Filtering; Table S3: Dominant Feature Loadings of Radiomic Principal Components Included in the Final Cox Model.

Author Contributions: Conceptualization, S.H.K. and J.L.; methodology, G.E.P. and E.J.M.; validation, S.H.H. and E.J.M.; formal analysis, E.J.M. and S.H.H.; investigation, G.E.P. and J.L.; resources, J.L. and S.H.K.; data curation, G.E.P. and E.J.M.; writing—original draft preparation, G.E.P.; writing—review and editing, S.H.K.; visualization, G.E.P.; supervision, S.H.K.; funding acquisition, J.L. All authors have read and agreed to the published version of the manuscript.

Funding: This study was supported by an investigator-initiated research grant from Bayer (Gadovist_18958). Bayer had no role in the study design; data collection, analysis, or interpretation; manuscript preparation; or the decision to submit this manuscript for publication. The authors retained full control of the study data and publication decisions. Apart from this institutional research funding disclosed above, the authors declare no relevant financial relationships with Bayer.

Institutional Review Board Statement: The study protocol was approved by the Institutional Review Board of Seoul St. Mary's Hospital (reference number: KC16EISI0425 and date of approval: February 2017). Written informed consent was obtained from all participants prior to enrollment in accordance with the principles of the Declaration of Helsinki.

Informed Consent Statement: Informed consent was obtained from all subjects involved in this study.

Data Availability Statement: Data supporting the findings of this study are available from the corresponding author on request, subject to institutional and ethical restrictions.

Conflicts of Interest: The authors declare no conflicts of interest.

Abbreviations

The following abbreviations are used in this manuscript:

YABC	Young-Age Breast Cancer
RFS	Recurrence-Free Survival
TNBC	Triple-Negative Breast Cancer
FGT	Fibroglandular Tissue
BPE	Background Parenchymal Enhancement
PCA	Principal Component Analysis

References

1. Leong, S.P.L.; Shen, Z.; Liu, T.; Agarwal, G.; Tajima, T.; Paik, N.; Sandelin, K.; Derossis, A.; Cody, H.; Foulkes, W.D. Is breast cancer the same disease in Asian and Western countries? *World J. Surg.* **2010**, *34*, 2308–2324. [CrossRef]
2. Sung, H.; Rosenberg, P.S.; Chen, W.Q.; Hartman, M.; Lim, W.; Chia, K.S.; Mang, O.W.-K.; Chiang, C.-J.; Kang, D.; Ngan, R.K.-C.; et al. Female breast cancer incidence among Asian and Western populations: More similar than expected. *J. Natl. Cancer Inst.* **2015**, *107*, djv107. [CrossRef]
3. Lim, Y.X.; Lim, Z.L.; Ho, P.J.; Li, J. Breast cancer in Asia: Incidence, mortality, early detection, mammography programs, and risk-based screening initiatives. *Cancers* **2022**, *14*, 4218. [CrossRef]
4. Paluch-Shimon, S.; Cardoso, F.; Partridge, A.H.; Abulkhair, O.; Azim, H.A.; Bianchi-Micheli, G.; Cardoso, M.; Curigliano, G.; Gelmon, K.; Gentilini, O.; et al. ESO–ESMO fifth international consensus guidelines for breast cancer in young women (BCY5). *Ann. Oncol.* **2022**, *33*, 1097–1118. [CrossRef]
5. Hu, X.; Myers, K.S.; Oluyemi, E.T.; Philip, M.; Azizi, A.; Ambinder, E.B. Presentation and characteristics of breast cancer in young women under age 40. *Breast Cancer Res. Treat.* **2021**, *186*, 209–217. [CrossRef]
6. Korean Statistical Information Service (KOSIS). Number of Cancer Cases, Relative Frequencies, Crude Incidence Rates, and Age-Standardized Incidence Rates for 24 Cancers/Gender. Available online: https://kosis.kr/index/index.do (accessed on 30 July 2025).
7. Lee, S.K.; Kim, S.W.; Yu, J.H.; Lee, J.E.; Kim, J.Y.; Woo, J.; Lee, S.; Kim, E.-K.; Moon, H.-G.; Ko, S.S.; et al. Is the high proportion of young age at breast cancer onset a unique feature of Asian breast cancer? *Breast Cancer Res. Treat.* **2019**, *173*, 189–199. [CrossRef]
8. Lee, H.B.; Han, W. Unique features of young age breast cancer and its management. *J. Breast Cancer* **2014**, *17*, 301–307. [CrossRef]
9. Mann, R.M.; Cho, N.; Moy, L. Breast MRI: State of the art. *Radiology* **2019**, *292*, 520–536. [CrossRef]
10. Aine, M.; Boyaci, C.; Hartman, J.; Häkkinen, J.; Mitra, S.; Campos, A.B.; Nimeus, E.; Ehinger, A.; Vallon-Christersson, J.; Borg, Å.; et al. Molecular analyses of triple-negative breast cancer in the young and elderly. *Breast Cancer Res.* **2021**, *23*, 20. [CrossRef]
11. Tzikas, A.K.; Nemes, S.; Linderholm, B.K. A comparison between young and old patients with triple-negative breast cancer: Biology, survival and metastatic patterns. *Breast Cancer Res. Treat.* **2020**, *182*, 643–654. [CrossRef]
12. Fu, J.; Wu, L.; Fu, W.; Tan, Y.; Xu, T.; Hong, Z.; Wang, F.; Li, S. How young is too young in breast cancer?—Young breast cancer is not a unique biological subtype. *Clin. Breast Cancer* **2018**, *18*, e25–e39. [CrossRef]
13. Brooks, J.D.; Christensen, R.A.G.; Sung, J.S.; Pike, M.C.; Orlow, I.; Bernstein, J.L.; Morris, E.A. MRI background parenchymal enhancement, breast density and breast cancer risk factors: A cross-sectional study in pre- and post-menopausal women. *npj Breast Cancer* **2022**, *8*, 97. [CrossRef]
14. King, V.; Gu, Y.; Kaplan, J.B.; Brooks, J.D.; Pike, M.C.; Morris, E.A. Impact of menopausal status on background parenchymal enhancement and fibroglandular tissue on breast MRI. *Eur. Radiol.* **2012**, *22*, 2641–2647. [CrossRef]
15. Corrias, G.; Micheletti, G.; Barberini, L.; Suri, J.S.; Saba, L. Texture analysis imaging: What a clinical radiologist needs to know. *Eur. J. Radiol.* **2022**, *146*, 110055. [CrossRef]
16. Satake, H.; Ishigaki, S.; Ito, R.; Naganawa, S. Radiomics in breast MRI: Current progress toward clinical application in the era of artificial intelligence. *Radiol. Med.* **2022**, *127*, 39–56. [CrossRef]
17. Wang, Z.; Wei, S. Diagnosing breast cancer subtypes using MRI radiomics and machine learning: A systematic review. *J. Radiat. Res. Appl. Sci.* **2025**, *18*, 101260. [CrossRef]
18. Chiacchiaretta, P.; Mastrodicasa, D.; Chiarelli, A.M.; Luberti, R.; Croce, P.; Sguera, M.; Torrione, C.; Marinelli, C.; Marchetti, C.; Domenico, A.; et al. MRI-based radiomics approach predicts tumor recurrence in ER+/HER2− early breast cancer patients. *J. Digit Imaging* **2023**, *36*, 1071–1080. [CrossRef]
19. Yu, Y.; Ren, W.; He, Z.; Chen, Y.; Tan, Y.; Mao, L.; Ouyang, W.; Lu, N.; Ouyang, J.; Chen, K.; et al. Machine learning radiomics of magnetic resonance imaging predicts recurrence-free survival after surgery and correlation of LncRNAs in patients with breast cancer: A multicenter cohort study. *Breast Cancer Res.* **2023**, *25*, 132. [CrossRef]
20. Xiong, L.; Tang, X.; Jiang, X.; Chen, H.; Qian, B.; Chen, B.; Lin, X.; Zhou, J.; Li, L. Automatic segmentation-based multi-modal radiomics analysis of US and MRI for predicting disease-free survival of breast cancer: A multicenter study. *Breast Cancer Res.* **2024**, *26*, 157. [CrossRef]
21. Xu, K.; Hua, M.; Mai, T.; Ren, X.; Fang, X.; Wang, C.; Ge, M.; Qian, H.; Xu, M.; Zhang, R. A multiparametric MRI-based radiomics model for stratifying postoperative recurrence in luminal B breast cancer. *J. Imaging Inform. Med.* **2024**, *37*, 1475–1487. [CrossRef]
22. Trombadori, C.; Boccia, E.; Tran, E.H.; Franco, A.; Orlandi, A.; Franceschini, G.; Carbognin, L.; Di Leone, A.; Masiello, V.; Marazzi, F.; et al. Role of radiomics in predicting early disease recurrence in locally advanced breast cancer patients: Integration of radiomic features and RECIST criteria. *Radiol. Med.* **2025**, *130*, 753–765. [CrossRef]
23. Yang, Y.; Liao, T.; Lin, X.H.; Ouyang, R.; Chen, Q.; Ma, J. Dual-region MRI radiomic analysis indicates increased risk in high-risk breast lesions: Bridging intratumoral and peritumoral radiomics for precision decision-making. *BMC Cancer* **2025**, *25*, 828. [CrossRef]

24. Yu, Y.; Ren, W.; Mao, L.; Ouyang, W.; Hu, Q.; Yao, Q.; Tan, Y.; He, Z.; Ban, X.; Hu, H.; et al. MRI-based multimodal AI model enables prediction of recurrence risk and adjuvant therapy in breast cancer. *Pharmacol. Res.* **2025**, *216*, 107765. [CrossRef]
25. Saha, A.; Harowicz, M.R.; Grimm, L.J.; Kim, C.E.; Ghate, S.V.; Walsh, R.; Mazurowski, M.A. A machine learning approach to radiogenomics of breast cancer: A study of 922 subjects and 529 DCE-MRI features. *Br. J. Cancer* **2018**, *119*, 508–516. [CrossRef]
26. Park, A.Y.; Han, M.R.; Seo, B.K.; Ju, H.Y.; Son, G.S.; Lee, H.Y.; Chang, Y.W.; Choi, J.; Cho, K.R.; Song, S.E.; et al. MRI-based breast cancer radiogenomics using RNA profiling: Association with subtypes in a single-center prospective study. *Breast Cancer Res.* **2023**, *25*, 79. [CrossRef]
27. Shiri, I.; Salimi, Y.; Mohammadi Kazaj, P.; Bagherieh, S.; Amini, M.; Saberi Manesh, A.; Zaidi, H. Deep radiogenomics sequencing for breast tumor gene-phenotype decoding using dynamic contrast magnetic resonance imaging. *Mol. Imaging Biol.* **2025**, *27*, 32–43. [CrossRef]
28. Nam, Y.; Park, G.E.; Kang, J.; Kim, S.H. Fully automatic assessment of background parenchymal enhancement on breast MRI using machine-learning models. *J. Magn. Reson Imaging* **2021**, *53*, 818–826. [CrossRef]
29. Park, G.E.; Kim, S.H.; Nam, Y.; Kang, J.; Park, M.; Kang, B.J. 3D breast cancer segmentation in DCE-MRI using deep learning with weak annotation. *J. Magn. Reson Imaging* **2024**, *59*, 2252–2262. [CrossRef]
30. Park, H.; Lim, Y.; Ko, E.S.; Cho, H.-H.; Lee, J.E.; Han, B.-K.; Ko, E.Y.; Choi, J.S.; Park, K.W. Radiomics signature on magnetic resonance imaging: Association with disease-free survival in patients with invasive breast cancer. *Clin. Cancer Res.* **2018**, *24*, 4705–4714. [CrossRef]
31. Wu, Z.; Lin, Q.; Fu, G.; Li, L.; Yue, Y.; Wang, H.; Chen, J.; Cui, C.; Su, X.; Bian, T. Pretreatment MRI-based radiomics for predicting recurrence and disease-free survival in young women with breast cancer after neoadjuvant chemotherapy. *J. Comput. Assist. Tomogr.* **2026**, *50*, 390–402. [CrossRef]
32. Lo Gullo, R.; Ochoa-Albiztegui, R.E.; Chakraborty, J.; Thakur, S.B.; Robson, M.; Jochelson, M.S.; Varela, K.; Resch, D.; Eskreis-Winkler, S.; Pinker, K. Development of an MRI radiomic machine-learning model to predict triple-negative breast cancer based on fibroglandular tissue of the contralateral unaffected breast in breast cancer patients. *Cancers* **2024**, *16*, 3480. [CrossRef]
33. Rizzo, S.; Botta, F.; Raimondi, S.; Origgi, D.; Fanciullo, C.; Morganti, A.G.; Bellomi, M. Radiomics: The facts and the challenges of image analysis. *Eur. Radiol. Exp.* **2018**, *2*, 36. [CrossRef]
34. Yin, L.; Duan, J.J.; Bian, X.W.; Yu, S. Triple-negative breast cancer molecular subtyping and treatment progress. *Breast Cancer Res.* **2020**, *22*, 61. [CrossRef]
35. Dent, R.; Trudeau, M.; Pritchard, K.I.; Hanna, W.M.; Kahn, H.K.; Sawka, C.A.; Lickley, L.A.; Rawlinson, E.; Sun, P.; Narod, S.A. Triple-negative breast cancer: Clinical features and patterns of recurrence. *Clin. Cancer Res.* **2007**, *13*, 4429–4434. [CrossRef]
36. Romond, E.H.; Perez, E.A.; Bryant, J.; Suman, V.J.; Geyer, C.E., Jr.; Davidson, N.E.; Tan-Chiu, E.; Martino, S.; Paik, S.; Kaufman, P.A.; et al. Trastuzumab plus adjuvant chemotherapy for operable HER2-positive breast cancer. *N. Engl. J. Med.* **2005**, *353*, 1673–1684. [CrossRef]
37. Piccart, M.; Procter, M.; Fumagalli, D.; de Azambuja, E.; Clark, E.; Ewer, M.S.; Restuccia, E.; Jerusalem, G.; Dent, S.; Reaby, L.; et al. Adjuvant pertuzumab and trastuzumab in early HER2-positive breast cancer in the APHINITY trial: 6 years' follow-up. *J. Clin. Oncol.* **2021**, *39*, 1448–1457. [CrossRef]
38. O'Flynn, E.A.M.; Morgan, V.A.; Giles, S.L.; DeSouza, N.M. Diffusion weighted imaging of the normal breast: Reproducibility of apparent diffusion coefficient measurements and variation with menstrual cycle and menopausal status. *Eur. Radiol.* **2012**, *22*, 1512–1518. [CrossRef]
39. Kim, J.Y.; Suh, H.B.; Kang, H.J.; Shin, J.K.; Choo, K.S.; Nam, K.J.; Lee, S.W.; Jung, Y.L.; Bae, Y.T. Apparent diffusion coefficient of breast cancer and normal fibroglandular tissue in diffusion-weighted imaging: The effects of menstrual cycle and menopausal status. *Breast Cancer Res. Treat.* **2016**, *157*, 31–40. [CrossRef]
40. Jung, Y.; Jeong, S.; Kim, J.Y.; Kang, D.K.; Kim, T.H. Correlations of female hormone levels with background parenchymal enhancement and apparent diffusion coefficient values in premenopausal breast cancer patients: Effects on cancer visibility. *Eur. J. Radiol.* **2020**, *124*, 108818. [CrossRef]
41. Iacconi, C.; Thakur, S.B.; Dershaw, D.D.; Brooks, J.; Fry, C.W.; Morris, E.A. Impact of fibroglandular tissue and background parenchymal enhancement on diffusion weighted imaging of breast lesions. *Eur. J. Radiol.* **2014**, *83*, 2137–2143. [CrossRef]

Disclaimer/Publisher's Note: The statements, opinions and data contained in all publications are solely those of the individual author(s) and contributor(s) and not of MDPI and/or the editor(s). MDPI and/or the editor(s) disclaim responsibility for any injury to people or property resulting from any ideas, methods, instructions or products referred to in the content.